

NGC6240: extended CO structures and their association with shocked gas [★]

C. Feruglio¹, F. Fiore², R. Maiolino³, E. Piconcelli⁴, H. Aussel⁵, D. Elbaz⁵, E. Le Floc'h⁵, E. Sturm⁶, R. Davies⁶, and C. Cicone³

¹ IRAM - Institut de RadioAstronomie Millimétrique 300 rue de la Piscine, Domaine Universitaire 38406 Saint Martin d'Hères, France, e-mail: feruglio@iram.fr

² INAF- Osservatorio astronomico di Roma, via Frascati 33, 00040 Monteporzio Catone, Italy

³ Cavendish Laboratory, University of Cambridge, 19 J. J. Thomson Ave., Cambridge CB3 0HE, UK

⁴ XMM-Newton Science Operations Centre, ESAC, P.O. Box 78, 28691 Villanueva de la Cañada (Madrid), Spain

⁵ Laboratoire AIM-Paris-Saclay, CEA/DSM/Irfu, CNRS, Université Paris Diderot, Saclay, pt courrier 131, 91191 Gif-sur-Yvette, France

⁶ Max-Planck-Institut für Extraterrestrische Physik (MPE), Giessenbachstr. 1, 85748 Garching, Germany

Received 4 June, 2012

ABSTRACT

We present deep CO(1-0) observations of NGC6240 performed with the IRAM Plateau de Bure Interferometer (PdBI). NGC6240 is the prototypical example of a major galaxy merger in progress, caught at an early stage, with an extended, strongly-disturbed butterfly-like morphology and the presence of a heavily obscured active nucleus in the core of each progenitor galaxy. The CO line shows a skewed profile with very broad and asymmetric wings detected out to velocities of -600 km/s and $+800$ km/s with respect to the systemic velocity. The PdBI maps reveal the existence of two prominent structures of blueshifted CO emission. One extends eastward, i.e. approximately perpendicular to the line connecting the galactic nuclei, over scales of ~ 7 kpc and shows velocities up to -400 km/s. The other extends southwestward out to ~ 7 kpc from the nuclear region, and has a velocity of -100 km/s with respect to the systemic one. Interestingly, redshifted emission with velocities 400 to 800 km/s is detected around the two nuclei, extending in the east-west direction, and partly overlapping with the eastern blue-shifted structure, although tracing a more compact region of size ~ 1.7 kpc. The overlap between the southwestern CO blob and the dust lanes seen in HST images, which are interpreted as tidal tails, indicates that the molecular gas is deeply affected by galaxy interactions. The eastern blueshifted CO emission is co-spatial with an $H\alpha$ filament that is associated with strong H_2 and soft X-ray emission. The analysis of Chandra X-ray data provides strong evidence for shocked gas at the position of the $H\alpha$ emission. Its association with outflowing molecular gas supports a scenario where the molecular gas is compressed into a shock wave that propagates eastward from the nuclei. If this is an outflow, the AGN are likely the driving force.

Key words. Galaxies: active – Galaxies: interaction – Galaxies: evolution – Galaxies: ISM – Galaxies: quasars – general

1. Introduction

The observed transformation of gas-rich star-forming galaxies into red, bulge-dominated spheroids devoid of gas, is due to several mechanisms. In massive galaxies star formation might lead to a faster gas consumption rate, compared to less massive ones (Daddi et al. 2007, Peng et al. 2010, Elbaz et al. 2011, Rodighiero et al. 2011). In addition, galaxy interactions, mergers (Sanders et al. 1988, Barnes & Hernquist 1996, Cavaliere & Vittorini 2000, Di Matteo et al. 2005), together with active galactic nuclei (AGN) and starburst feedback are expected to play a role (Silk & Rees 1999, King 2010 and references therein). Mergers can destabilize cold gas and trigger both star formation and nuclear accretion onto super-massive black holes (SMBHs), inducing AGN activity. A natural expectation of this scenario is that the early, powerful AGN phase is highly obscured by large columns of gas and dust (e.g. Fabian 1999). Once a SMBH reaches masses $> 10^{7-8} M_{\odot}$, the AGN can efficiently contribute

to the radiative heating of the inter stellar medium (ISM) through winds and shocks, thus inhibiting further accretion and also star-formation in the nuclear region and possibly at larger scales in the galactic disk. The radiative feedback from a luminous AGN is therefore a mechanism that could explain the low gas content of local massive galaxies and the galaxy bimodal color distribution (Kauffmann et al. 2003, Croton et al. 2006, Menci et al. 2006). This evolutionary scenario needs to be observationally confirmed. This can be achieved by observing systems during a major interaction phase, that probe both AGN and starburst-driven winds, and their interaction with the molecular gas, which represents the bulk of the gas in a galaxy.

Only recently molecular gas outflows have been discovered in both star-forming galaxies (e.g. M82, Walter et al. 2002, Arp 220, Sakamoto et al 2009) and in the hosts of powerful AGN, through the detection of both molecular absorption lines with P-Cygni profiles, and of broad molecular emission lines (Feruglio et al. 2010, Fisher et al 2010, Alatalo et al. 2011, Sturm et al. 2011, Aalto et al. 2012, Cicone et al. 2012, Maiolino et al. 2012). The inferred outflow rates show that these outflows can displace large amounts (several hundreds of solar masses per year) of molecular gas into the galactic disk, hence support-

[★] This work is based on observations carried out with the IRAM Plateau de Bure Interferometer. IRAM is supported by INSU/CNRS (France), MPG (Germany) and IGN (Spain). This work is also based on observations performed with the Chandra X-ray Observatory.

ing AGN feedback model predictions (e.g. King 2005, 2010, Zubovas & King 2012, Lapi et al. 2005, Menci et al. 2008). In particular, strong molecular outflows have been found in several local Ultra Luminous Infrared Galaxies (ULIRGs), suggesting that they might be common in objects undergoing major mergers (Sturm et al. 2011). The "prototype" of this class of objects is Mrk 231, in which we indeed discovered a massive molecular outflow extended on scales of ~ 1 kpc in the host galaxy disk (Feruglio et al. 2010). Mrk231 is known to be in a late merger state (Sanders et al. 1988, Davies et al. 2005), and shows a compact molecular disk (Carilli et al. 1998).

In the framework of the exploration of massive molecular outflows in nearby ULIRGs and LIRGs, we present in this work our millimeter observations of the nearby merger NGC6240. This is a prototypical galaxy undergoing transformations. Thanks to its close distance ($z=0.024$), this system offers the opportunity to investigate in detail the distribution and dynamics of the molecular gas during a merger event, which represents the key process in hierarchical models of galaxy formation and evolution. It is a massive object, resulting from the merger of two gas rich spirals. The nuclei, separated by $\sim 2''$ in approximately the north-south direction, are located in the central region of the system, probably the remnants of the bulges of the progenitor galaxies, since the majority of the nuclear stellar luminosity is provided by stars predating the merger (Engel et al. 2010). Each nucleus hosts an AGN (Komossa et al. 2003). At least one of the AGN is highly obscured by a hydrogen column density of $N_H > 10^{24} \text{ cm}^{-2}$ (Compton-thick), and has an intrinsic luminosity $L(2-10 \text{ keV}) > 10^{44} \text{ erg s}^{-1}$ (Vignati et al. 1999). The mass of the SMBH powering this AGN likely exceeds $10^8 M_\odot$ (Engel et al. 2010). The system is in an early, short-lived phase of merging, likely between the first encounter and the final coalescence, as witnessed by intense star-formation activity (see e.g. Sanders & Mirabel 1996, Mihos & Hernquist 1996). The system thus has a greater physical size with respect to Mrk231, and exhibits large scale streamers and outflows, witnessed by the spectacular butterfly-shaped emission-line nebula seen in HST H α images (Gerssen et al. 2004). The nebula is interpreted as evidence of a super-wind shock-heating the ambient ISM. The emission line filaments and bubbles appear to trace a bipolar outflow pattern, aligned east-westward, extending up to 15-20 arcsec (7-10 kpc) from the nuclear region perpendicular to the wide dust lane seen in the HST images (Gerssen et al. 2004), and to the line connecting the two nuclei. The superwind is likely powered by both the nuclear star-formation and by the AGN. NGC6240 is thus an ideal target to study: a) the interplay between AGN and star-formation activity; b) the mechanism of transport of energy from the nuclei to the gas in the outer parts of the galaxy; c) how the molecular gas is heated by the winds.

We present in this work CO(1-0) maps obtained with the IRAM Plateau de Bure Interferometer (PdBI) in the D and A array configurations. These data have lower spatial resolution than previous works (Engel et al. (2010), Iono et al. (2007), Nakanishi et al. (2005)), but the useful bandwidth is much broader and the noise level is a factor > 2 lower. We also present a reanalysis of the Chandra X-ray, high spatial resolution data (available from the Chandra public archive). A Λ CDM cosmology ($H_0 = 70 \text{ km s}^{-1} \text{ Mpc}^{-1}$; $\Omega_M=0.3$; $\Omega_\Lambda = 0.7$) is adopted.

2. PdBI observations and data analysis

We observed with the PdBI the CO(1-0) transition, redshifted to 112.516 GHz assuming a systemic velocity of 7339 km/s (Iono et al. 2007), corresponding to a redshift of $z=0.02448$. The ob-

servations were carried out in May 2011 with six antennas using the compact array configuration, and in January 2012 with 5 antennas in the extended (A) configuration. The on-source time of this dataset is ~ 4.6 hr in the compact configuration, and ~ 5.9 hr in the extended configuration.

Data reduction was performed using GILDAS. The system temperatures during the observations were in the range between 150 and 300 K. The absolute flux calibration relies on the strong quasars 3C273 and 3C279 and its accuracy is expected to be of the order 10% (Castro-Carrizo & Neri 2010). The synthesized beams, obtained by using natural weighting, are $5.6'' \times 4.6''$ for the D configuration and $1.4'' \times 0.7''$ for the A configuration maps. The achieved noise levels are 0.9 and 1.2 mJy/beam over 20 MHz (i.e. ~ 50 km/s) for the D configuration data, and configuration A data, respectively.

3. X-ray observation and data analysis

NGC6240 was observed by Chandra on July 2001 for about 35 ksec. Reduced and calibrated data are available from the public CXO data archive. Results from these observations have been published by Komossa et al. (2003), and Lira et al. (2004).

4. Results

Figure 1 shows the continuum-subtracted spectrum of the CO(1-0) line, extracted from a polygonal region enclosing the source from the D array configuration data. The 3 mm continuum was estimated by averaging the visibilities in the spectral channels corresponding to the velocity ranges -3500 to -2000 km/s, and 2000 to 4000 km/s with respect to the systemic velocity. This range of velocities (not shown in Fig. 1 for clarity) is fully covered by the WideC Correlator and it is free from emission lines. Based on the data taken in the D array configuration, the continuum emission peaks at $-0.16, 0.82$ arcsec off the phase tracking center, and has a flux density of 12.7 mJy. This is consistent with the 1 mm continuum reported by Tacconi et al. (1999), assuming a radio spectral index of 0.7. Two components of the radio and mm continua, centered at the position of each AGN, are found in maps with higher spatial resolution (Tacconi et al. 1999, Colbert et al. 1994). Our data from the D configuration do not allow to spatially resolve these two components. The continuum map shows one component whose fitted size is $1 \pm 0.1 \text{ kpc}$ (FWHM), assuming a circular gaussian model. The 1 mm and radio (8 GHz) continua are consistent with non thermal synchrotron emission. The CO line peaks close to the assumed systemic velocity (~ -50 km/s). Broad and asymmetric wings extend to at least -600 km/s on the blue side and $+800$ km/s on the red side of the line peak. The full width at zero intensity (FWZI ~ 1400 km/s) is broader than that of CO(2-1) and CO(3-2) reported by Engel et al. (2010) and Iono et al. (2007). In particular, the blue side of the line covers a larger velocity range than the previously reported -450 km/s (Bryant & Scoville 1999, Tacconi et al. 1999, Engel et al. 2010, Iono et al. 2007, Nakanishi et al. 2005), probably due to the larger bandwidth and the better sensitivity of the new PdBI receivers.

Figure 2 shows the integrated maps from the D configuration data of the CO core emission (-50 to 50 km/s) and of the red-shifted velocities (from 400 to 800 km/s with respect to the systemic velocity). The axes show the coordinate offsets with respect to the phase tracking center, (ra, dec)=(16:52:58.9, 02:24:02.9). The positions of the two AGN nuclei from VLBI observations (Hagiwara et al. 2011) are indicated by crosses. The

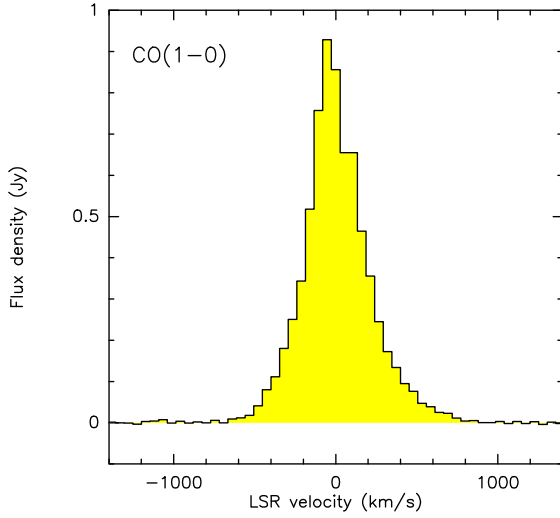


Fig. 1. CO(1-0) spectrum of NGC6240 obtained with IRAM/PdBI in D configuration. Asymmetric broad wings extend from -600 km/s to $+800$ km/s with respect to the systemic velocity. The 3 mm continuum has been subtracted in order to highlight the high velocity wings. The spectral channels are 53.3 km/s wide.

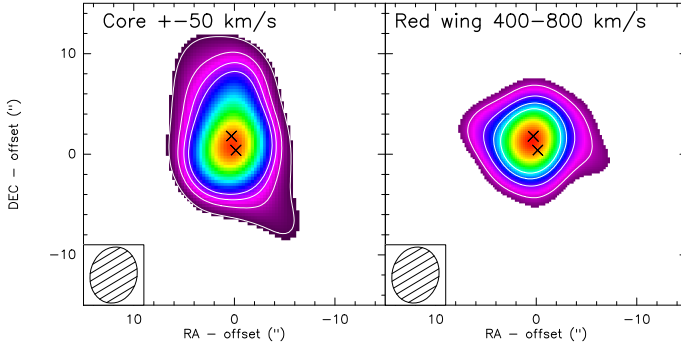


Fig. 2. Maps of the CO core emission (left panel, -50 , $+50$ km/s) and red wing emission (400 to 800 km/s with respect to the systemic velocity), from the compact D array data. Each contour is 5σ (limited to 20σ). The positions of the two AGN nuclei are shown by crosses. The synthesized beam is shown in the bottom-left corners.

CO core emission is elongated in the north-south direction on scales of $10''$, and shows a faint south-western elongation. The map of the red wing shows a strong compact source, of size ~ 1.7 kpc, co-spatial with the narrow core emission, and an elongation in the east-west direction with a position angle of 80 degrees. Fitting an elliptical gaussian model in the uv plane gives a flux of 11.4 Jy km/s for this high velocity, red-shifted component. The uv-fit results are reported in Table 1.

4.1. Blue-shifted CO emission

We now examine in detail the blue-shifted emission of CO. We find complex morphology, extended on scales from a few arcseconds to 15 - $20''$. Figure 3 shows CO(1-0) maps at different velocities, from -400 to -100 km/s in channels 20 MHz ($=53.3$ km/s) wide, for the D and A configuration data. Each contour in Fig. 3 is 5σ (limited to 20σ for clarity). Two structures are particularly prominent: emission extended eastward out to at least $15''$ with velocities from -400 to -200 km/s, and emission ex-

tending southwestward with velocities from -200 to -100 km/s. The most prominent emission is located eastward from the nuclei, i.e. approximately perpendicular to the line connecting the galactic nuclei, in the velocity range -400 to -150 km/s. From this, a structure showing velocities of ~ -260 km/s develops in the southern direction, likely a tidal tail remnant of the merger. This shows substructure, in the form of three main clumps of CO emission, and it coincides with the smooth structure seen by Bush et al. (2008) at $8 \mu\text{m}$, and tracing dust through emission by poly-aromatic hydrocarbons (PAHs). Figure 3 (lower panels) shows the maps obtained by merging the data from the D and A configuration. The synthesized beam is intermediate between those of the two and allows for better spatial resolution of the thin, jet-like structures, to better follow their alignment with the emission at other wavelengths. In the merged maps, we estimate, that for the central region (around the nuclei) we are missing $\sim 33\%$ of the flux.

Figure 4 shows two spectra extracted from circular regions of $2''$ radius centered on the eastern and southwestern features. The spectra were extracted from the cleaned data cubes in regions that enclose the extended structures shown in Fig. 3. These spectra are presented for the purpose of showing the emission line peak velocity and line-width, and should not be used to derive the fluxes. Here we derive the line fluxes from the visibilities of D configuration data. We derive the line intensities of the two blue-shifted structures and of the nuclear region by fitting in the uv-plane the visibilities of the compact D configuration array data. The fit in the uv-plane yields the flux at zero-spacing. First, we fit the central region around the two nuclei (see Fig. 2, left panel), with the combination of two elliptical gaussian models, which yield a line intensity $I_{\text{CO}} = 213$ Jy km/s. The results of the fit are reported in Table 1. The fit produces a residual table where the visibilities of the central component have been subtracted. To derive the line intensity of the blue-shifted, extended structures, we fit the residual visibilities using two elliptical gaussians. The derived line intensity is 49.3 Jy km/s (over 600 km/s) for the eastern emission region, and 32.5 Jy km/s (over 400 km/s) for the south-western streamer. Summing these three components, we obtain a total integrated CO intensity of 295 ± 29 Jy km/s, in agreement with both Solomon et al. (1997) single dish observations (310 Jy km/s), and with the interferometric flux (324 Jy km/s) of Bryant & Scoville (1999).

Note that the emission of each blue-shifted region is 4 to 7 times fainter than the central part of the galaxy. As seen in Fig. 3, both these structures are spatially resolved. The eastern component is found $7.6''$, $1.3''$ off the phase tracking center. The southwestern one is found at $-6.4''$, $-6.8''$ off the phase center. The fit with elliptical gaussians gives sizes of $14.4'' \times 8.2''$ for the eastern blob, and $8.3'' \times 4.4''$ for the southwestern blob.

Figure 5 (left panel) shows the Wide Field Planetary Camera (WFPC2 F673N) image from the Hubble Space Telescope (HST), which includes the galaxy's $\text{H}\alpha$ emission (Gerssen et al. 2004), with overlaid contours of the blue-shifted CO(1-0) emission at -400 km/s and -100 km/s. The WFPC2 image shows that the $\text{H}\alpha$ nebula comprises five main bright filaments: two southwards of the nuclear region, one located in the western region, and two eastwards from the nuclei. We note that the CO emission with velocity -100 km/s is located on the southwestern dust lane, in between two $\text{H}\alpha$ filaments. An elongation of this component toward the northern dust lane is also visible. The CO emission centered at -400 km/s first follows the eastern elongation of the $\text{H}\alpha$ emission, and continues further eastward and southward. We also show the X-ray emission at 1.6 - 2 keV, centered on the highly ionized Si emission (white contours). Note

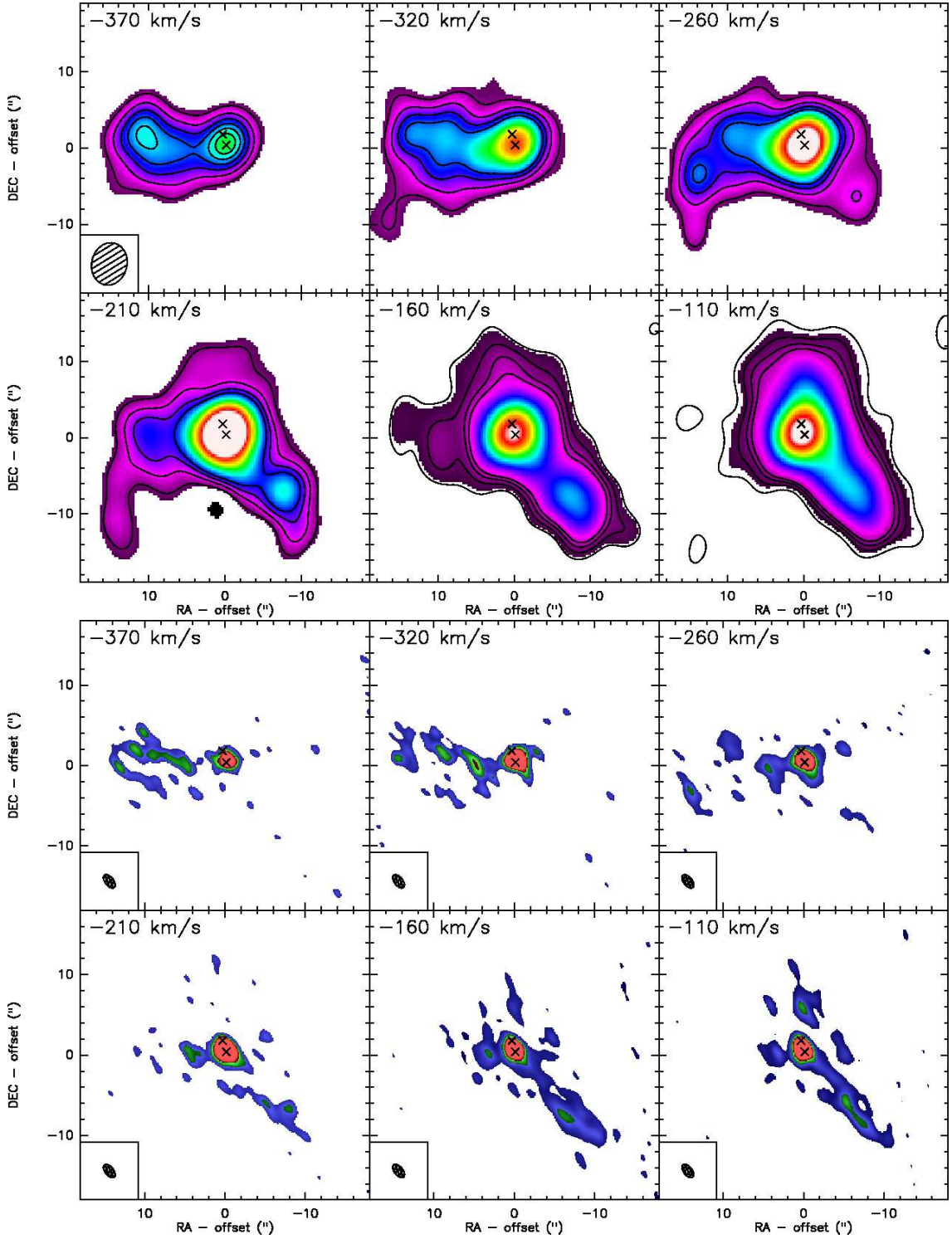


Fig. 3. Upper panel: CO(1-0) maps from the compact array data, in velocity bins of 20 MHz each (velocity labels are rounded off), showing the detection of blue-shifted CO, including structures extended on scales of 10-15". The positions of the two AGN nuclei are shown by crosses. The synthesized beam is shown on the first panel only, for clarity. Each contour is 5σ (limited to 20σ). Lower panel: maps from merged data of the D and A configurations in the same velocity channels. The synthesized beams are shown in the bottom-left corners.

that the X-ray data trace remarkably well the $H\alpha$ emission. In particular, the soft X-ray emission is coincident with the eastern $H\alpha$, H_2 (see fig. 9 in Max et al. 2005) and CO elongation. This leads us to investigate further the association of the X-ray emission with the $H\alpha$, H_2 and CO emitting gas.

4.2. X-ray spatially resolved spectroscopy

We extracted a spectrum from the X-ray Chandra data at the position of each of the five $H\alpha$ filaments described above, and combined them. The extraction regions are shown in Figure 6. A background spectrum has been extracted from a source free

Table 1. Measured quantities from the uv-plane fit, and derived quantities (line luminosities and gas masses) of the CO emitting components.

Spectral Component	RA [J2000]	DEC [J2000]	S_ν [mJy]	SIZE ["]	PA [deg]	FWZI [km/s]	I_{CO} [Jy km/s]	$L(\text{CO})$ [$10^9 \text{ K km s}^{-1} \text{ pc}^2$]	$M(\text{H}_2)$ [$10^9 M_\odot$]
Nuclear	16 : 52 : 58.90	02 : 24 : 04.16	138.3 ± 0.8	4.7×3.4	0.4	1400	213	5.7	4.5
Red wing	16 : 52 : 58.93	02 : 24 : 04.35	28.5 ± 0.7	3.4×2.4	81	400	11.4	0.3	0.15
Blue-E	16 : 52 : 59.41	02 : 24 : 04.34	82.1 ± 5	14.4×8.2	-65	600	49.3	1.3	0.7
Blue-SW	16 : 52 : 58.47	02 : 23 : 56.15	81.3 ± 2	8.3×4.4	38	400	32.5	0.87	0.43

Notes. Data were fitted with elliptical gaussian models in the uv-plane on the continuum-subtracted visibilities. Errors are of statistical nature and do not account for the uncertainties in the absolute flux calibration. This is conservatively expected to be of the order 10%.

region at distances of 2 to 5 arcmin from the nuclei of the galaxy of 25 arcmin^2 size, in order to avoid the contamination from the diffuse X-ray emission, which is still seen on scales of 1 arcmin away from the nuclei. The background-subtracted X-ray spectrum is plotted in Fig. 7. Strong emission lines are visible at about 1.3-1.4 keV, 1.7-1.9 keV and 2.3-2.4 keV. At these energies the ionized emission from Mg, Si and S is expected. We fitted the spectrum using XSPEC and adopting χ^2 statistics. The spectrum was binned to have at least 30 counts per channel. We limited the fit to the 0.5-7 keV band (440 original channels, 67 bins), where the instrument response is best calibrated and to avoid strong background lines at high energy (see e.g. the Chandra background spectrum in Fiore et al. 2011). We started modeling the spectrum with a thermal equilibrium gas component (MEKAL in XSPEC), reduced at low energy by photoelectric absorption by gas along the line of sight. This model is clearly inadequate to reproduce the observed spectrum, giving a $\chi^2=179.5$ for 63 degrees of freedom (DOF) and large residuals at 0.8-0.9 keV, 1.2 keV, 1.8 keV and above 4 keV. We then added a second thermal equilibrium gas component to the model. Figure 7 shows the best fit model with 8 free parameters (two temperatures, two metal abundances, two normalizations and two absorbing column densities). The best fit χ^2 is 93.3 (59 DOF). Note the rather strong positive residuals at 1, 1.4, 1.8, 2.2 keV, i.e. the position of the Mg, Si, and S line complexes. Stronger

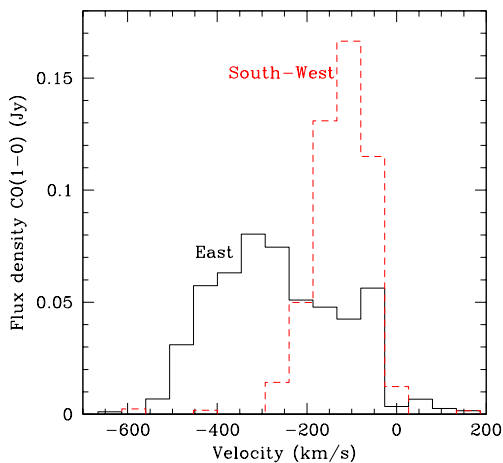


Fig. 4. CO(1-0) spectra of NGC6240 extracted from the D configuration data in circular regions of $2''$ radii encompassing the extended, blue-shifted emission eastward (solid black histogram) and southwestward of the nuclei (red dashed histogram). The extraction regions are centered at offsets of $(7.6'', 1.3'')$ and $(-6.4'', -6.8'')$ from the phase tracking center.

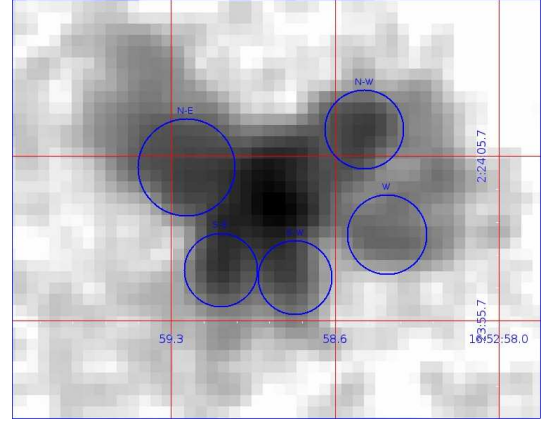


Fig. 6. The Chandra X-ray map of NGC 6240 in the energy range 0.3-4 keV. The circles indicate the regions where we extracted the X-ray spectra. The region for the background extraction is outside the limits of this map, at 2-5 arcmin from the nuclei.

line emission is expected in non-equilibrium models, because of the broader ion distribution with respect to thermal equilibrium models at the same temperature and metal abundances. In particular, shock models, like XSPEC PSHOCK are known to produce spectra with prominent line emission. We therefore fitted the spectrum with a model including a thermal equilibrium component and a shock component. The best fit χ^2 is now 62.1 (58 DOF). The improvement in χ^2 with respect to the two component thermal equilibrium model is significant at the 99.9997% confidence level (using the F test). Residuals with respect to the best fit model do not show any systematic deviation. Figure 8 shows the best fit unfolded (i.e. corrected for the response matrix of the instrument) spectrum with the identified contributions of the thermal equilibrium and shock components. We conclude that the X-ray analysis supports the idea that shocked gas is present at the position of strong $\text{H}\alpha$ emission, both in the nuclear starburst and in the elongated filaments.

5. Discussion and conclusions

We have obtained deep 3 mm maps of the archetypical interacting galaxy NGC6240 with the IRAM PdBI, covering a velocity range of 10.000 km/s. The CO(1-0) line shows strong blue and red wings extending from -600 km/s to $+800 \text{ km/s}$ with respect to the systemic velocity. The line (FWZI= 1400 km/s) is significantly broader than that previously reported by Tacconi et al. (1999), Engel et al. (2010), and Iono et al. (2007). The systemic CO emission shows a north-south elongation over at least $10''$. Elongation in the same direction is seen in the CO(1-0) maps of Bryant & Scoville (1999), and in the CO(2-

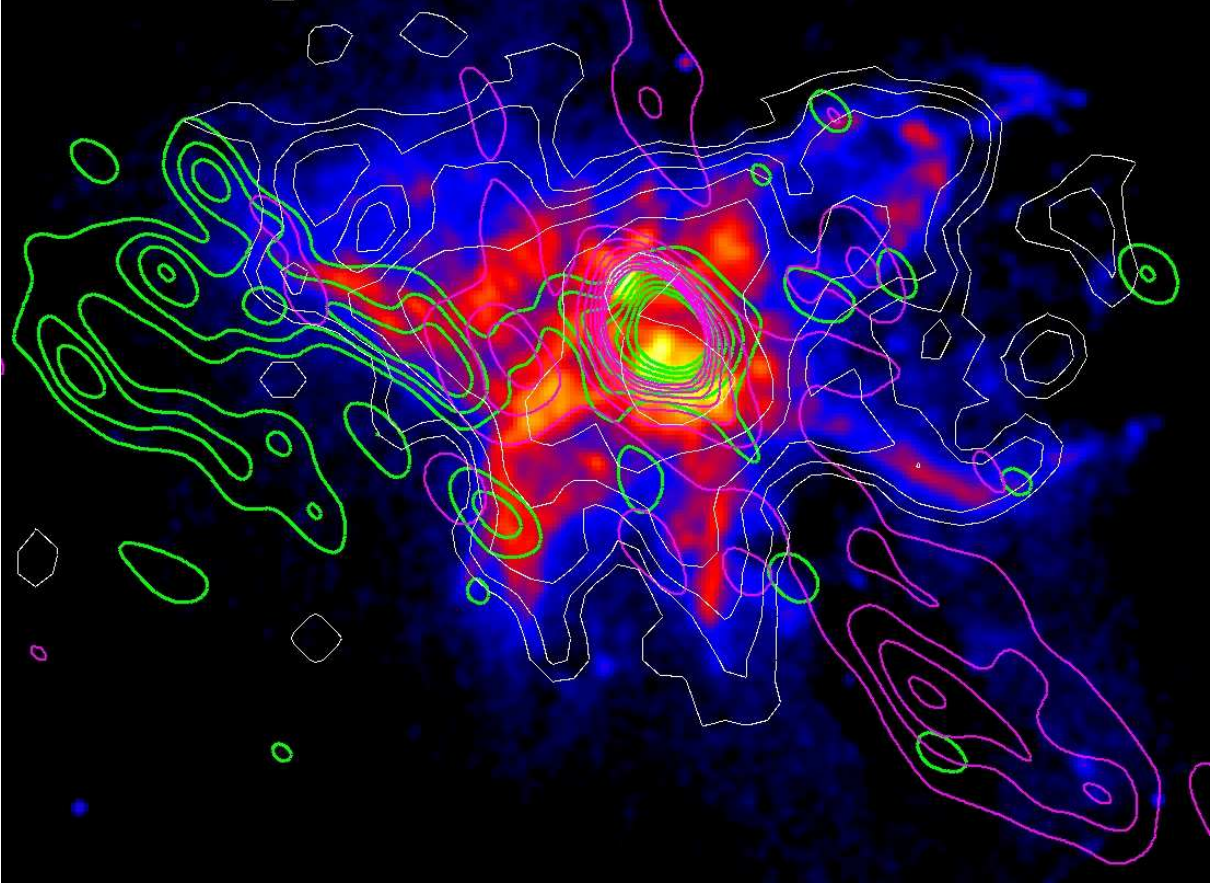


Fig. 5. $H\alpha$ map of NGC6240 (color image). CO(1-0) emission at different velocities: -350 km/s (green contours), -100 km/s (magenta contours), with respect to the system velocity. Contours are calculated by merging D and A configuration data. Chandra 1.6-2 keV emission is shown by white contours.

1) maps of Tacconi et al. (1999), and Engel et al. (2010) on 10 times smaller scales. The CO luminosity of this region is $L'(\text{CO}) = 5.7 \times 10^9 \text{ K km s}^{-1} \text{ pc}^2$. We derive an estimate of the molecular gas mass in this region, assuming the standard CO to H_2 conversion factor, $\alpha = 0.8 \text{ M}_\odot (\text{K km s}^{-1} \text{ pc}^2)^{-1}$ (units omitted hereafter). We find $M(\text{H}_2) = 4.5 \times 10^9 \text{ M}_\odot$, consistent with the value derived from CO(2-1) for this region by Tacconi et al. (1999).

We were able to identify new components. We find CO emission extended up to distances of $15\text{-}20''$ from the galaxy centers ($7\text{-}10$ kpc at the distance of NGC6240). In particular, we find strong emission blue-shifted by ~ 150 to 400 km/s extending eastward by at least $15''$ from the nuclei, and by $100\text{-}200$ km/s extending south-westward on a similar scale. The presence of the latter component was suggested by the interferometric CO maps of Bryant & Scoville (1999), although with low significance.

The CO southwestern emission coincides with the dust lane seen in HST images (Gerssen 2004, also see Fig. 5) and in the IRAC $8 \mu\text{m}$ image (Bush et al. 2008). This large scale dust distribution has been interpreted as due to a tidal tail curving in front of the system (Gerssen et al. 2004, Yun & Hibbard 2001). Molecular gas is associated with this tidal tail, a situation reminiscent of M82, where Walter et al. (2002) found molecular gas in the tidal tails correlated with dust absorption features. The integrated CO luminosity of the southwestern emitting region is $L'(\text{CO}) = 8.7 \times 10^8 \text{ K km s}^{-1} \text{ pc}^2$. For the conversion from CO luminosity into molecular gas mass $M(\text{H}_2)$, we conservatively adopted the lowest conversion factor found in the giant outflows

and streamers of M82 (Weiss et al. 2001), $\alpha = 0.5$. The mass of the molecular gas in this region is thus $M(\text{H}_2) = 4.3 \times 10^8 \text{ M}_\odot$, 4-to-10 times the H_2 mass in the streamers of M82 (Walter et al. 2002, derived for the same conversion factor). This estimate likely represents a lower limit to the molecular gas mass in this streamer. The physical size of the southwestern tidal tail is however at least $15''$, i.e. 7 kpc, 4-7 times larger than the streamers in M82 (Walter et al. 2002). The CO extended emission to the north (see Fig.2, left panel) coincides with a dust lane seen in HST images (Gerssen et al. 2004), and might be associated with another streamer. The detection of molecular streamer(s) in NGC6240 confirms that the molecular gas is severely affected by galaxy interaction, and that the redistribution of molecular gas is likely the trigger for the strong starburst activity in the central region of NGC6240.

The blueshifted eastern CO emitting region is not associated with the dust lanes mentioned above, but follows a $H\alpha$ filament, and PAH emission observed at $8 \mu\text{m}$ (Bush et al. 2008). The emission-line nebula seen in $H\alpha$ images (Gerssen et al. 2004) is interpreted as evidence of a superwind that is shock heating ambient ISM. The $H\alpha$ emitting filaments are aligned east-westward, perpendicular to the dust lanes and to the line connecting the two nuclei. The X-ray emission is associated with the $H\alpha$ filaments (Lira et al. 2002). In particular, strong soft X-ray emission is coincident with the north-eastern filament (N-E region in Fig. 6). We re-analyzed the Chandra X-ray data and found strong evidence for shocked gas at the position of the $H\alpha$ filaments. The presence of shocked gas in the NGC6240 system

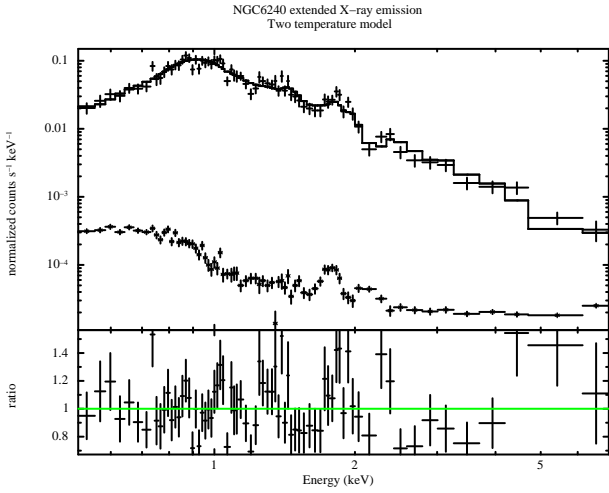


Fig. 7. Top panel: the top curve represents the background corrected Chandra spectrum (uncorrected for the response of the instrument; crosses denote spectral widths and amplitude uncertainties) extracted at the position of H α filaments (see Fig. 6), and fitted with a two-temperature thermal equilibrium model (solid line). The lower curve represents the background spectrum. Data, represented by crosses, have been binned to give a signal to noise ratio > 5 in each bin (for plotting purposes only). Bottom panel: the data to model ratio (the green solid line representing a ratio of unity). Note the residuals at about 1 keV, 1.4 keV, 1.8 keV, 2.2 keV and 5 keV.

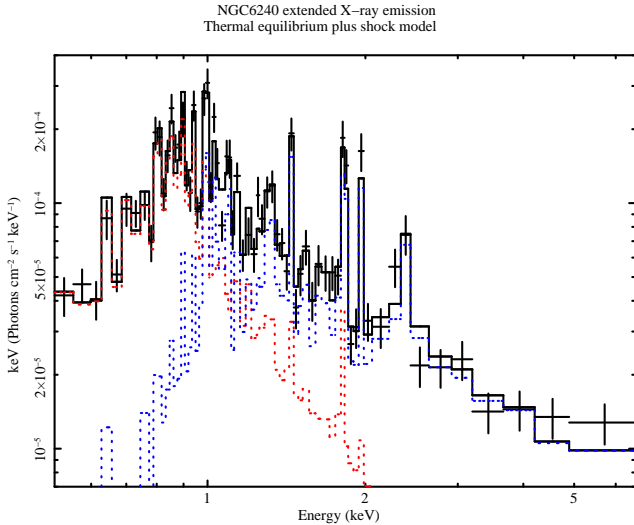


Fig. 8. The background corrected Chandra spectrum (also corrected for the response matrix of the instrument) extracted at the position of the H α filaments (see Fig. 6). Symbols are as in Fig. 7. Red dotted histogram: thermal equilibrium model component; blue dashed histogram: shock model component.

is confirmed by the detection of strong H $_2$ (1-0) S(1) emission at 2.12 μm . NGC6240 has the strongest H $_2$ line emission found in any galaxy (Goldader et al. 1995). Shocks are usually identified as the excitation mechanism for this line. Ohyama et al. (2000, 2003) suggest that such shocks are produced by a superwind outflowing from the southern nucleus and colliding with the surrounding molecular gas. Intriguingly, Max et al. (2005) find that excited H $_2$ emission closely follows the H α filament extending eastward. Note that the position of one of the peaks

of the eastern blue-shifted CO emission coincides with the position where Bland-Hawthorne et al. (1991) and Gerssen et al. (2004) found a large velocity gradient of the ionized gas (the velocity decreasing, roughly, north to south). No significant radio continuum emission is detected in this region in the VLA maps of Colbert et al. (1994). The blue-shifted molecular gas in this region might be a tidal tail, left behind during the merger. However, its association with strongly shocked gas suggests that a shock is propagating eastward and is compressing also the molecular gas, while crossing it.

The integrated luminosity of CO in this region is $L'(\text{CO}) = 1.3 \times 10^9 \text{ K km s}^{-1} \text{ pc}^2$, corresponding to a gas mass $M(\text{H}_2) = 7 \times 10^8 M_\odot$ (assuming again $\alpha = 0.5$). Hypothesizing that this outflow originates from the southern, luminous AGN (or from both the AGN), we derive here a mass loss rate. We assume that the molecular outflow is distributed in a spherical volume of radius $R_{\text{of}} = 7 \text{ kpc}$ (i.e. the distance of the eastern blob from the AGN), centered on the AGN. If the gas is uniformly distributed in this volume, the volume-averaged density of molecular gas is given by $\langle \rho_{\text{of}} \rangle = 3 M_{\text{of}} / \Omega R_{\text{of}}^3$, where Ω is the solid angle subtended by the outflow and M_{of} is the mass of gas in the outflow (Feruglio et al. 2010, Maiolino et al. 2012). This assumption is an approximation, and evidently cannot represent the complexity of the system, but can provide a rough estimate of the mass loss rate. Based on this geometry, we can derive a mass loss rate by using the relation:

$$\dot{M}(\text{H}_2) \sim v \Omega R_{\text{of}}^2 \langle \rho_{\text{of}} \rangle = 3 v \frac{M_{\text{of}}}{R_{\text{of}}}$$

where v is the terminal velocity of the outflow ($\sim 400 \text{ km/s}$). This relation yields a mass loss rate of $\dot{M} \sim 120 M_\odot/\text{yr}$. The H α , H $_2$ and CO(1-0) maps suggest that the outflow is most likely conical. In this geometry, since the mass loss rate is independent of Ω , the mass outflow rate would be equal to the spherical case if there are no significant losses through the lateral sides of the cone. As it is observed in other local massive outflows (Cicone et al. 2012, Aalto et al. 2012), the outflowing gas is likely characterized by a large range of densities, ranging from low density gas to dense clumps, which would increase the mass flow rate. In addition, the mass flow rate would obviously be larger than our previous estimates if α is significantly higher than 0.5. To date, this is the lowest conversion factor measured in an extragalactic object. This said, it is unlikely that the mass loss rate is smaller than several tens $M_\odot \text{ yr}^{-1}$, and it is likely as big as a few hundreds $M_\odot \text{ yr}^{-1}$. The kinetic power of the outflowing gas is given by the relation $P_k = 0.5 v^2 \dot{M} = 6 \times 10^{42} \text{ erg s}^{-1}$. The age of the outflow is $> 2 \times 10^7$ years, since it is observed at about 7 kpc distance from the southern nucleus. The star-formation rate at the position of the eastern filament can be evaluated through both the H α luminosity and the X-ray luminosity (e.g. Kennicutt 1998, Ranalli et al. 2003). The 0.5-2 keV X-ray luminosity at the position of the East filament is $0.5 - 1 \times 10^{41} \text{ erg s}^{-1}$, which according to Ranalli et al. (2003) would imply a star-formation rate of $10-20 M_\odot \text{ yr}^{-1}$. This estimate is derived by assuming that all the X-ray luminosity is due to star-formation. In section 4.2 we showed that at least a fraction of the X-luminosity is due to a shock, therefore the SFR derived from the X-ray is an upper limit. This would suggest that the outflow is not pushed by SN winds. Indeed, the power transferred to the ISM by a star-formation driven wind is given by $P_{\text{SF}} = \eta \times 7 \times 10^{41} \times \text{SFR} = 10^{42} \text{ erg s}^{-1}$, where $\eta \sim 0.1$ is the standard mass-energy conversion (see e.g. Lapi et al. 2005). We conclude that it is unlikely that the molecular flow is powered by star-formation. Instead, star-formation in this region is likely in the process of being quenched by the outflow.

However, we cannot exclude that star-formation in this area is induced by the compression caused by the propagating shock.

We detected a red-shifted component with velocity 400 to 800 km/s with respect to the systemic velocity (Fig. 2), centered around the two AGN nuclei. Interestingly this emitting region is elongated in the same east-west direction as the blue-shifted emission discussed above, although on smaller scales (~ 1.7 kpc in diameter). We derive a CO luminosity of this component of $L'(\text{CO}) = 3.0 \times 10^8 \text{ K km s}^{-1} \text{ pc}^2$, which converts into a gas mass of $M(\text{H}_2) = 1.5 \times 10^8 M_\odot$, under the same assumptions given above for the CO-to- H_2 conversion factor. The large velocity of this component suggests that the AGN might contribute to the dynamics of this gas (Sturm et al. 2011).

Given the complex dynamics and morphology of this system, it is not trivial to disentangle and quantify the relative role of each mechanism. Probably several mechanisms are acting contiguously: mainly the radiation pressure of the AGN together with dynamic shocks induced by the merger event. High resolution, X-ray observations will help to clarify the interaction between the star-forming regions and the CO extended structures (Wang et al. in preparation, conference communication). The high spatial resolution data taken in the A array configuration indeed provide new insights on the nuclear region, which will be addressed in a separate publication (Feruglio et al. 2012, in preparation).

Acknowledgements. We thank D. Downes and R. Neri for useful inputs and careful reading of the paper. F.F. acknowledges support from PRIN-INAF 2011. We acknowledge the referee for her/his very careful review, that allowed us to significantly improve the quality of this work.

References

- Aalto, S. et al. 2012, A&A 537, 44
 Alatalo, K. A. et al. 2011, ApJ, 735, 88
 Barnes, J. E. & Hernquist, L. 1996, ApJ 471, 115
 Bland-Hawthorne, J. et al. 1991, ApJ 375, 19
 Boroson, T., & Meyers, K. 1992, ApJ, 397, 442
 Bryant, P. M., & Scoville, N. Z. 1996, ApJ, 457, 678
 Bush, S. J. et al. 2008, ApJ, 688, 875
 Carilli, C. L., Wrobel, J. M., & Ulvestad, J. S. 1998, AJ, 115, 928
 Castro-Carrizo, A. & Neri, R. 2010, IRAM Plateau de Bure Interferometer Data Reduction Cookbook
 Cavaliere, A. & Vittorini, V. 2000, ApJ 543, 599
 Ciccone, C. et al. 2012, A&A in press, arXiv:1204.5881C
 Colbert, E. J. M., Wilson, A. S. & Bland-Hawthorn, J. 1994, ApJ, 436, 89
 Croton, D. J. et al. 2006, MNRAS 367, 864
 Daddi, E. et al. 2007, ApJ 670, 173
 Davies, R. I. et al. 2005, ApJ 633, 105
 Davies, R. I., Tacconi, L. J., & Genzel, R., 2004, ApJ, 613, 781
 Dekel, A. et al. 2009, Nature, 457, 451
 Di Matteo, T., Springel, V. & Hernquist, L. 2005, Nature, 433, 604
 Downes, D. & Solomon, P. M., ApJ, 507, 615
 Elbaz, D. et al. 2011, A&A 533, 119
 Engel, H. et al. 2010, A&A 524, 56
 Fabian, A. C., 1999, MNRAS, 308, 39
 Feruglio, C. et al. 2010, A&A 518, 155
 Fiore, F. et al. 2012, A&A 537, 16
 Fischer, et al., 2010, A&A,
 Gerksen, J. et al. 2004, AJ, 127, 75
 Granato, G. L., De Zotti, G., Silva, L., et al. 2004, ApJ, 600, 580
 Goldader, J. D. et al. 1995, ApJ 444, 97
 Hagiwara, Y. et al. 2011, AJ 142, 17
 Iono, D. et al. 2007, ApJ, 659, 283
 Kauffmann, G. et al. 2003, MNRAS, 346, 1055
 Kennicutt, R. C. 1998, ApJ 498, 541
 King, A. R. 2005, ApJ, 635, 121
 King, A. R. 2010, MNRAS, 402, 1516
 Komossa, S. 2003, ApJ 582, 15
 Lapi, A. et al. 2005, ApJ 619, 60
 Lira, P. et al. 2002, MNRAS, 330, 259
 Maiolino, R. et al. 2012, MNRAS in press, arXiv:1204.2904
 Max, C. E. et al. 2005, ApJ 621, 738
 Menci, N., Fontana, A., Giallongo, E., et al. 2006, ApJ, 647, 753
 Menci, N., Fiore, F., Puccetti, S. & Cavaliere, A. 2008, ApJ, 686, 219
 Mihos, J. C. & Hernquist, L. 1996, ApJ 464, 641
 Nakanishi, K. et al. 2005, PASJ, 57, 575
 Ohyama, Y. et al. 2000, PASJ, 52 563
 Ohyama, Y. et al. 2003, AJ 126, 229
 Peng, Y. et al. 2010, ApJ 721, 193
 Ranalli, P., Comastri, A. & Setti, G. 2003, A&A 399, 39
 Rodighiero, G. et al. 2011, ApJ 739, 40
 Sakamoto, K. et al. 2009, ApJ 700, 104
 Sanders, D. B., et al., 1988, ApJ, 325, 74
 Sanders, D. B. & Mirabel, I.F. 1996 ARA&A, 34, 749
 Scoville, N. Z., Frayer, D. T., Schinnerer, E. & Christopher, M. 2003, ApJ, 585, L105
 Silk, J. & Rees, M. J. 1998, A&A, 331, L1
 Sturm, E. et al. 2011, A&A 518, 36
 Solomon, P. M. et al. 1997, ApJ 478, 144
 Solomon, P.M., Downes, D., Radford, S.J.E., Barret, J.W. 2007, ApJ, 478, 144
 Solomon, P. M., & Vanden Bout, P. A. 2005, ARA&A, 43, 677
 Tacconi, L. et al. 1999, ApJ 524, 732
 Veilleux, S. et al. 2005, ARA&A, 43, 769
 Vignati, P. et al. 1999, A&A 349, 57
 Yun, M. S., & Hibbard, J. E. 2001, in Gas and Galaxy Evolution, ed. J. E. Hibbard, M. Rupen, & J. H. van Gorkom, ASP Conf. Proc., 240, 866
 Walter, F. et al. 2002, ApJ 580, 21
 Weiss, A., Neininger, N., Hüttemeister, S., & Klein, U. 2001, A&A, 365, 571
 Zubovas, K. & King A. 2012, ApJ, 745, 34